3.2 2-section Wavelength Monitor

An inline quauntum-well photodetector based device was first proposed by Wu *et al* [11]. The incoming light is coupled into the waveguide which consists of a pair of inline photodiodes (Figure 3.2). A fraction of this incoming light is absorbed in the first section, and the rest is transmitted through to the second section where it gets absorbed. These photocurrents generated by this absorption in the two sections can be measured. Near the material's band-edge, its transparency goes from opaque to transparent as the wavelength increases. This means that, for shorter wavelengths, the light will be absorbed more in the first section and for longer wavelengths, the light will travel further to the second section, making the ratio of the photocurrents a very sensitive indicator of the wavelength as shown in figure 3.3.

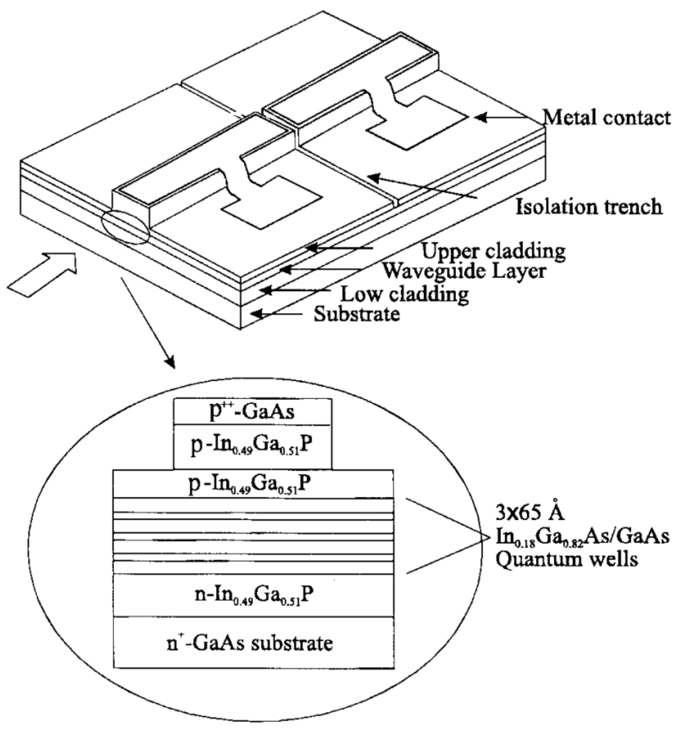

Figure 3.2: An inline quantum well photodetector based device for wavelength monitoring[11]

The following section outlines the theory behind the operation of this two section wavelength monitor.

3.2.1 Theory of operation

To calculate the photocurrents generated in a waveguide photodetector we define Responsivity, $\mathcal{R}$, which is the generated photocurrent per unit of optical power, as follows [12]

$$\mathcal{R} = \frac{I}{P} = \frac{e}{h\nu}\eta_{ext} \tag{3.1}$$

where I is the generated photocurrent, P is the optical power, η_{ext} is the external quantum efficiency and h is the Planck's constant and ν is the optical frequency. In terms of the wavelength of light, Equation 3.1 can be written as:

$$\mathcal{R} = \frac{e\lambda}{hc}\eta_{ext} \tag{3.2}$$

The external quantum efficiency, η_{ext} can be written as [12]:

$$\eta_{ext} = \frac{\Gamma\alpha^{int}}{\alpha}\eta(1 - e^{-\alpha L}) \tag{3.3}$$

where Γ is the optical confinement factor, α^{int} is the interband absorption coeefficient of the quantum wells, L is the waveguide length, η is the internal quantum efficiency and α is the total loss coeffecient of the propagating mode through the waveguide. Assuming the device is operating in a standalone setting, the coupling coefficient κ into the waveguide from an external fibre and the reflection of the facet, R, can be included in equation 3.3 and can be rewritten as:

$$\eta_{ext} = \kappa(1 - R)\frac{\Gamma\alpha^{int}}{\alpha}\eta(1 - e^{-\alpha L}) \tag{3.4}$$

Combing equations 3.2 and 3.4, the generated photocurrent is given by:

$$I = \frac{e\lambda}{hc}P\kappa(1 - R)\frac{\Gamma\alpha^{int}}{\alpha}\eta(1 - e^{-\alpha L}) \tag{3.5}$$

Considering a multi segment photodetector, the optical power reaching the i'th segment, P_i is given by:

$$P_i = Pe^{-\sum\limits_{k=1}^{i-1}\alpha_k(\lambda)L_k} \tag{3.6}$$

where P is the input optical power and α_k and L_k are the absorption coefficient and the length of the k'th segment respectively. Combining equations 3.5 and

3.6, we obtain the generated photocurrent in the i'th segment as:

$$I_i = \frac{e\lambda}{hc} P\kappa(1-R)\eta \frac{\Gamma\alpha^{int}(\lambda)}{\alpha(\lambda)} e^{-\sum_{k=1}^{i-1}\alpha_k(\lambda)L_k}(1-e^{-\alpha_i(\lambda)L_i}) \tag{3.7}$$

Considering a two segment photodetector with equal lengths, ignoring any scattering losses between the two sections, and assuming a single pass of the optical field with negligible reflection from the back facet, the photo-currents in the front (I_{front}) and rear (I_{rear}) sections can be written, from equation 3.7, as

$$\begin{aligned} I_{front} &\propto \lambda(1-e^{-\alpha(\lambda)L}), \\ I_{rear} &\propto \lambda(1-e^{-\alpha(\lambda)L})e^{-\alpha(\lambda)L} \end{aligned} \tag{3.8}$$

and the photocurrent ratio between the two sections is given by

$$\frac{I_{rear}}{I_{front}} = e^{-\alpha(\lambda)L} \tag{3.9}$$

Using Urbach's empirical rule [13] for $\alpha(\lambda)$ near the band edge,

$$\alpha(\lambda) \propto e^{\left(\frac{E(\lambda)-E_g}{kT}\right)} \tag{3.10}$$

the photocurrents obtained from equations 3.8 and 3.9 are plotted in Figures 3.3(a) and 3.3(b) respectively, where $E(\lambda)$ is the photon energy, E_g is the bandgap, k is Boltzmann's constant and T is the temperature.

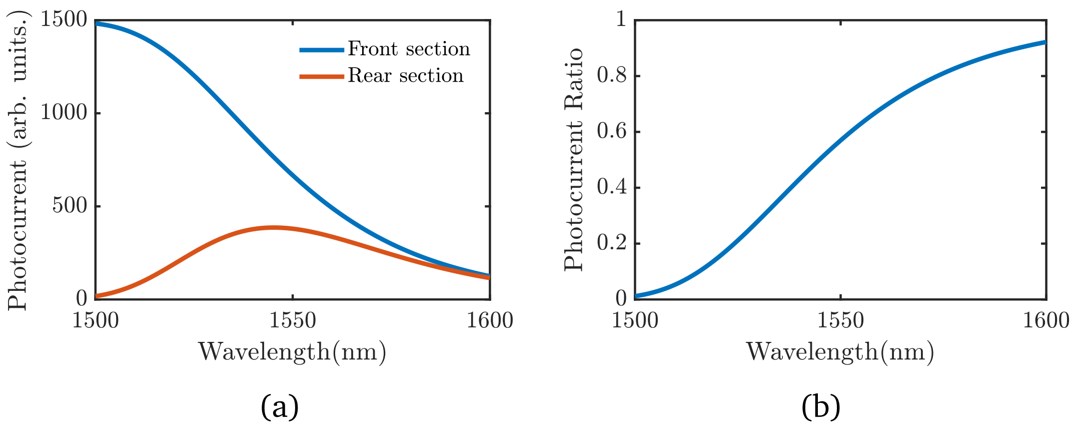

Figure 3.3: (a) Photocurrents in the two sections and (b) Photocurrent ratio calculated theoretically in a 2-section wavelength monitor

From equation 3.9 it is evident that this photocurrent ratio is independent of many factors such as input optical power, coupling efficiency, facet reflections and dependent only on the absorption coefficient and the lengths of the photodetector segments. Since the absorption coefficient α is strongly dependent on the wavelength near the band edge, this ratio provides a sensitive measure of the wavelength. However, it is important to note that this relation of the photocurrent ratio to the band edge could lead it to be dependent on polarisation, since the epitaxial material structure could have different band edges for different optical polarisations.

3.2.1.1 Sensitivity analysis

In the previous section, the physics behind the ideal performance of a 2-section wavelength monitor was discussed. When it comes to practical use in the real world, non-idealities in the device must also be considered.

In a scenario where the two sections of the device would have asymmetric response to the incident optical field, the photocurrent ratio will be affected. For example, an unbalanced electrical leakage current in the two sections or unsaturable waveguide losses will a wavelength-independent term in the expression for photocurrent in equation 3.7. Accounting for this, the simulated photocurrents and the photocurrent ratio are plotted in Figure 3.4 (a) and (b) respectively.

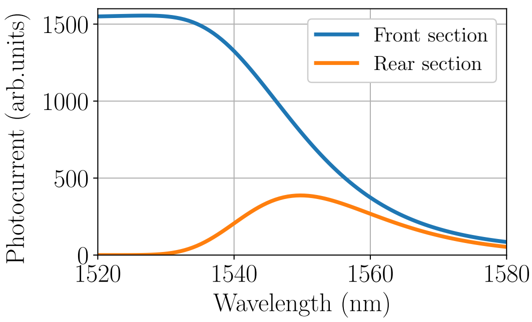

(a)

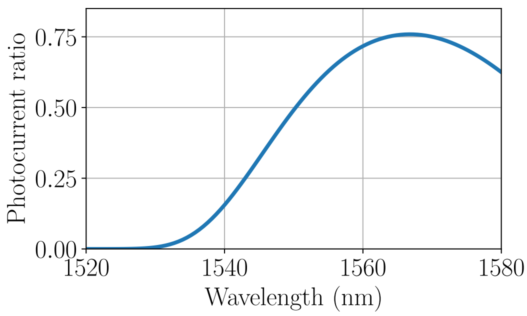

(b)

Figure 3.4: (a) Photocurrents in the two sections and (b) Photocurrent ratio calculated theoretically with a non-ideal asymmetry between the two sections

This non-ideality causes the photocurrents in the two sections not to converge at longer wavelengths and in turn the photocurrent ratio experiences a roll-off. Although it is interesting to understand this scenario, the actual operating wavelength range in our case is below this roll-off. Hence, this would not affect the performance of the wavelength monitor adversely. The other important factor to consider is the operating temperature of the device. The bandgap of the quantum well materials shifts with temperature and this results in change in the absorption spectrum $\alpha(\lambda)$ in equation 3.10. The shift in bandgap with temperature can be modelled using the relation proposed by Varshni[14]:

$$E_g(T) = E_g(0) - \frac{\gamma T^2}{T + \delta} \tag{3.11}$$

Substituting values for the parameters $E_g(0) = 0.811$, $\gamma = 3.4 \times 10^{-4}$ and $\delta = 50$ from literature[15] for InGaAsP/InP into equation3.11 and plugging in the resulting $E_g(T)$ into equation3.10, we can simulate the photocurrent ratio for different temperatures as shown in Figure 3.5 (a).

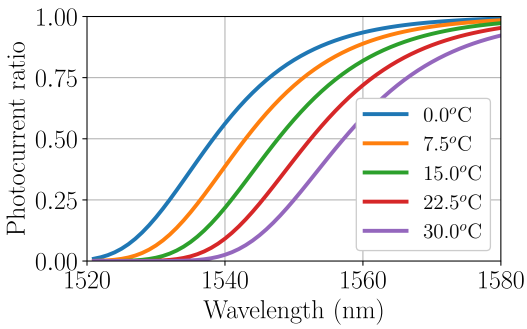

(a)

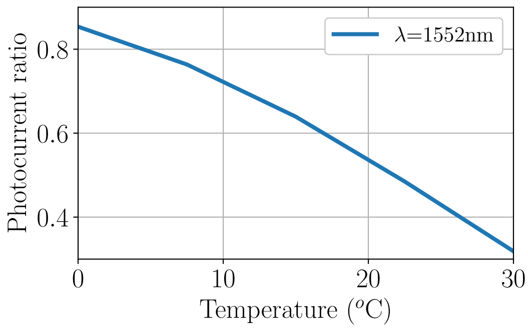

(b)

Figure 3.5: Photocurrent ratio as a function of (a) wavelength for different temperatures (b) temperature for a particular wavelength

We observe that the photocurrent ratio curve shifts to longer wavelengths with increase in temperature. This is to be expected since the bandgap decreases, i.e. shifts to longer wavelengths with increase in temperature. For a constant wavelength (1552 nm), the photocurrent ratio is plotted versus temperature in Figure 3.5 (b). Approximating a linear behaviour, the ratio changes by about 0.018 per degree Celsius. This translates into a wavelength 'error' of about 0.5 nm or 62 GHz which is a very considerable amount. We can conclude from this analysis that temperature control of this device is of critical importance.

Other than temperature, the bandgap of the quantum well material is also different for different polarisations of the incident optical field. This polarisation dependence of the bandgap is a function of the nature and amount of strain the the quantum well layers. This means that, in theory, it could be possible to get rid of the polarisation dependence of the wavelength monitor if we could engineer a correct amount of tensile strain on the wells to match the TE and

TM bandgaps with each other.

3.2.2 Standalone Performance

The 2-section wavelength monitor was fabricated using the process described in Chapter 2 as a standalone device. Light from an Agilent 81600B Tuneable Laser Source (TLS) was passed through a polarisation controller to select pure TE polarised light was injected into the device via a lensed fibre. The two sections of the device were biased at 0 Volts and the generated photocurrents were read out using a Keithley SourceMeter®. The schematic of this measurement setup is shown in Figure 3.6. The wavelength of the TLS was swept keeping the optical power constant at a value of 1mW and the resulting photocurrents and the photocurrent ratio are plotted in Figure 3.7. Comparing this with Figure 3.3, we can see good agreement between the theoretical and experimentally obtained performance of the wavelength monitor. Additionally comparing with Figure 3.4, we observe the the currents in the two sections not converging to the same value thus resulting in a rollover for the photocurrent ratio as predicted by the simulations described in the previous section.

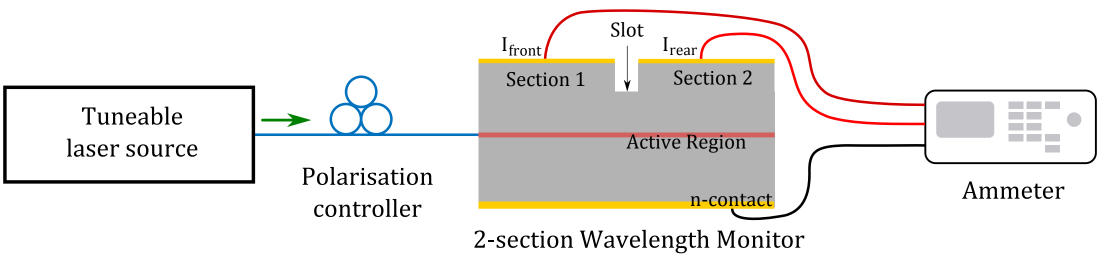

Figure 3.6: Schematic of the measurement setup

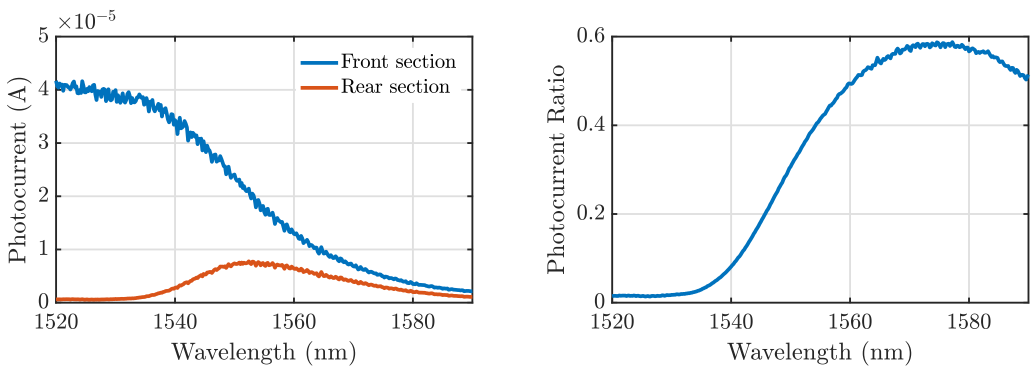

(a) (b)

Figure 3.7: (a) Photocurrents from front and rear sections and (b) Ratio of photocurrents as a function of wavelength

According to equation 3.9, the photocurrent ratio is theoretically independent of optical input power. This was tested and plotted in Figure 3.8. We observe that while the photocurrents in the individual sections go down as the input power decreases, the ratio between them remains constant and thus independent of the optical power, thus making it a robust indicator for sensing the input wavelength. Once again, the rollover behaviour at longer wavelengths is observed in the same proportion for all optical powers, hinting that this rollover is most probably caused by as asymmetrical electrical leakage current between the two sections.

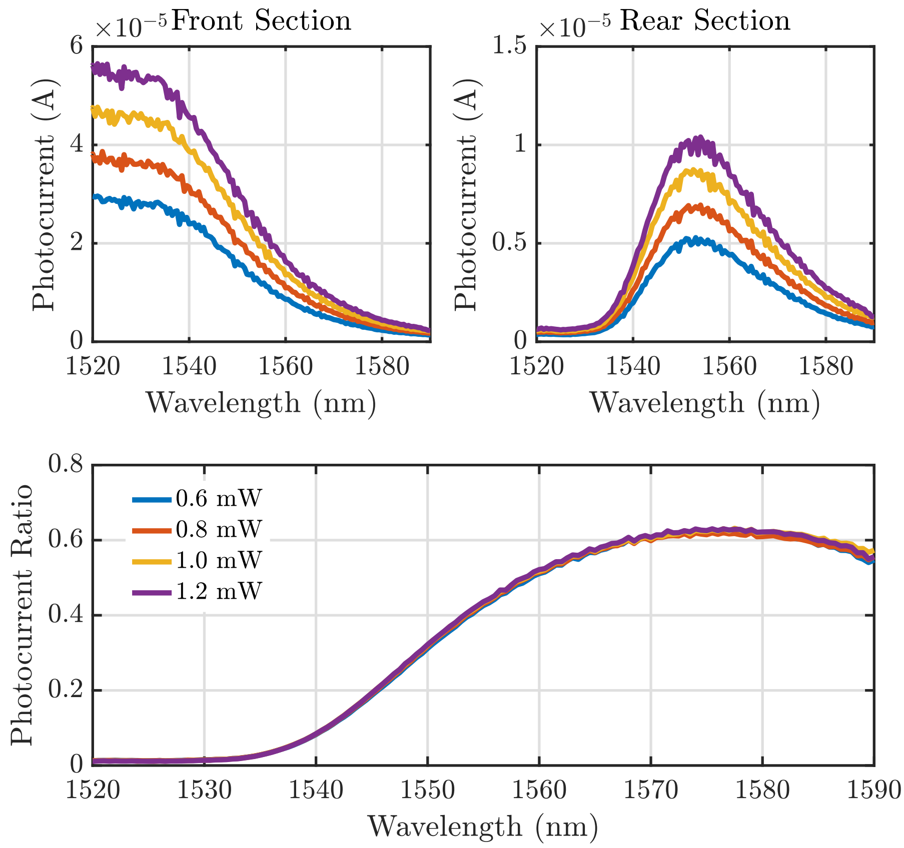

Figure 3.8: Readouts from the wavelength monitor as a function of input optical power

The wavelength-tuneable slotted Fabry-Perót laser described Chapter 2 and the wavelength monitor described in the section above were mounted on separate butterfly packages. The light was coupled between them using a single mode optical fibre. The tuneable laser was placed on a mount with a thermoelectric cooler (TEC). As the wavelength of the laser is tuned using its drive currents, the photocurrents in the wavelength monitor are read out and fed into a LabVIEW™ program. This program then sets the temperature of the TEC mount underneath the laser accordingly, which fine-tunes and stabilises the lasing wavelength. The schematic of this setup is shown in Figure 3.9, and the readout from the wavelength monitor is shown in Figure 3.11. The red curve is the value of the photocurrent ratio theoretically resulting from the setting of the wavelength of the tuneable laser. The laser was tuned between three diferent wavelengths λ_1, λ_2 and λ_3 which were 1546.18nm, 1546.3nm and 1546.58nm respectively. The black curve shows the measured value of the photocurrent ratio resulting from the stabilisation of the laser using a PID controller in the feedback loop. There is evident ringing in the photocurrent ratio, and thus the wavelength. The main reason for this is the slow response of the thermal feedback implementation resulting from a double PID loop: one in LabVIEW and one within the TEC (model number) which sets the temperature using its internal PID controller. In practice, it would be theoretically possible to optimise this using custom-made electronics for the feedback loop between heating and the photocurrent ratio, resulting in wavelength stabilisation times of around milliseconds. Additionally from the noise in the photocurrent ratio, it can be inferred that the wavelength can be stabilised with a precision of 0.12nm (ex: λ_1 and λ_2) or about 15 GHz.

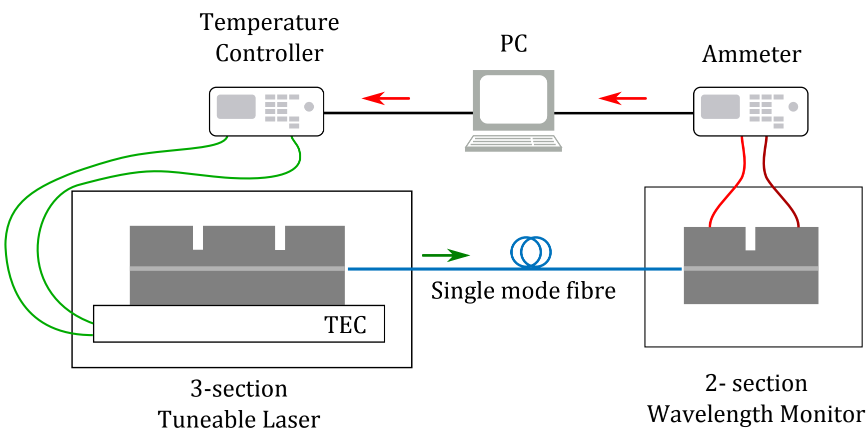

Figure 3.9: Schematic of the wavelength stabilisation setup

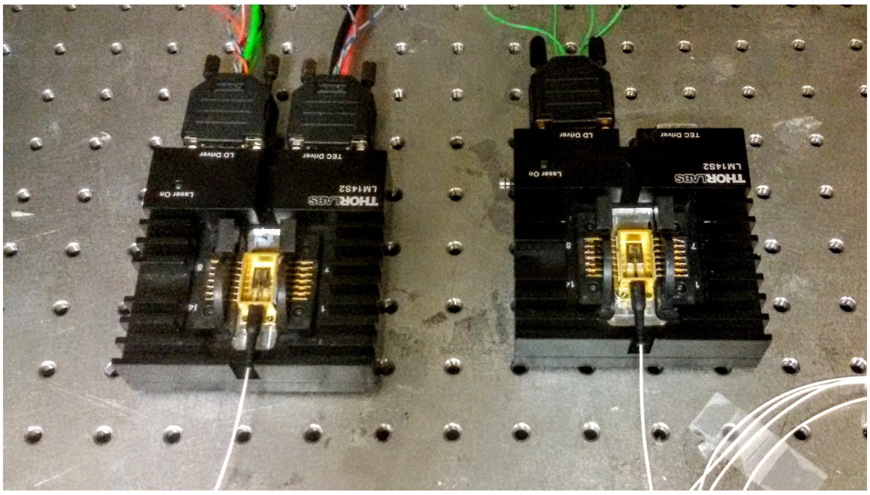

Figure 3.10: Photograph of a 3-section tuneable laser and a 2-section wavelength monitor mounted in separate butterfly packages

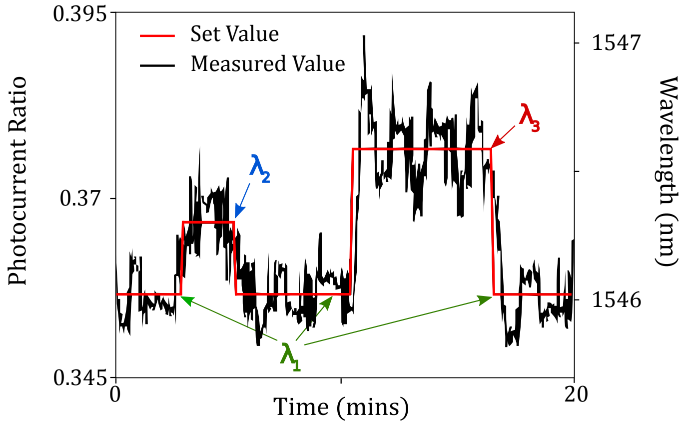

Figure 3.11: Photocurrent ratio from the wavelength monitor for three different wavelengths

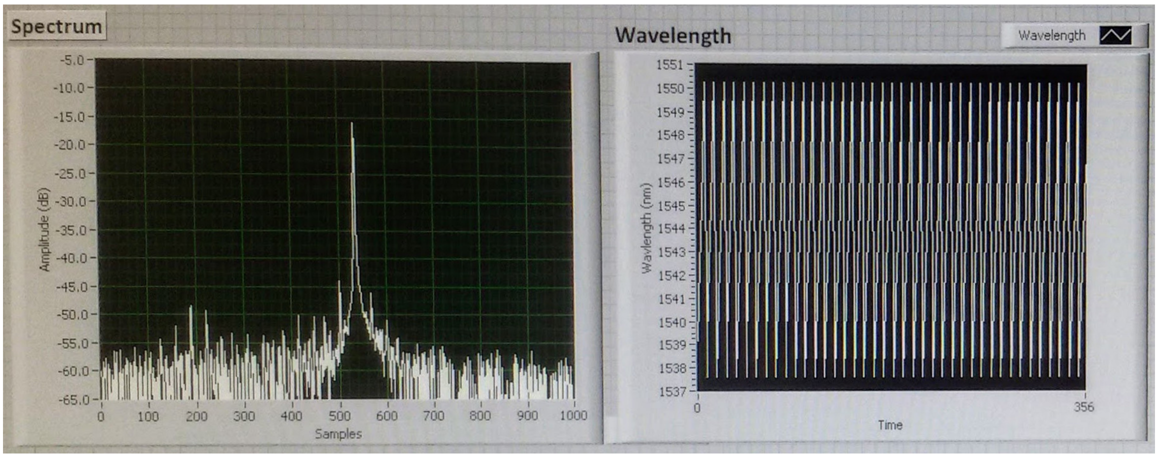

(a) (b)

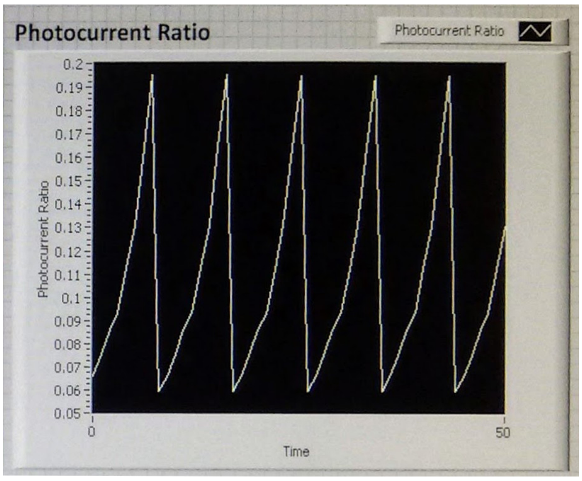

(c)

Figure 3.12: Screenshots from LabVIEW™of (a) (b) and (c)